RECENT RESULTS ON B DECAYS
FROM CLEO

Ahren Sadoff

Ithaca College

Cornell University

Representing the CLEO Collaboration

ABSTRACT

CLEO, concentrating on the $\Upsilon(4s)$ resonance at CESR, has accumulated an integrated luminosity corresponding to 2×10^6 produced $B\overline{B}$ pairs. This has allowed us to investigate a wide variety of B-decay processes. In this paper, I will concentrate on three general decay modes: semileptonic decays, two-body nonleptonic decays, and rare hadronic decays. The recent measurement of the inclusive $b \rightarrow s\gamma$ branching fraction will be discussed in some detail.

Table of Contents

1   Introduction

1.1 Physics at the $\Upsilon(4s)$

The CLEO collaboration, made up of about 220 physicists from 22 institutions, has concentrated on studying the $\Upsilon(4s)$ resonance since it is just above threshold for producing B mesons. Figure 1 shows the hadronic cross section as a function of center-of-mass energy, W, in the Υ region. The cross section $\sigma(\Upsilon(4s) \to B\bar{B})$ is 1.07 nb at W=10.58 GeV. The continuum cross section below the resonance $\sigma(e^+e^- \to q\bar{q})$ is approximately 3 nb.

CLEO has currently accumulated an integrated luminosity of $2fb^{-1}$ on the $\Upsilon(4s)$ which is equivalent to 2×10^6 produced $B\bar{B}$ pairs. In addition, approximately $1fb^{-1}$ has been accumulated on the continuum at an energy slightly below the $\Upsilon(4s)$. CESR, the Cornell Electron Storage Ring, has operated at a peak luminosity of 2.5×10^{32} $cm^{-2} sec^{-1}$. The "best day" integrated luminosity, so far, has been 14.4 pb^{-1}.

1.2 Event Selection

For most analyses, the $q\bar{q}$ continuum is the major source of background. There are several commonly used variables that are employed to reduce the contribution from the continuum. They are based on the difference in shapes between $B\bar{B}$ and $q\bar{q}$ events. At the $\Upsilon(4s)$, the produced B mesons are almost at rest so the distribution of decay particles tends to be spherical. On the other hand, the $q\bar{q}$ events tend to be jetty.

Two variables which can distinguish event shapes have been found to be quite useful. The normalized second Fox-Wolfram moment, R_2, has a range from 0 to 1. It is large for $q\bar{q}$ events and small for $B\bar{B}$ events. The second variable is $\cos\theta_t$, where θ_t is the angle between the candidate thrust axis and the thrust axis of the rest of the event. The distribution for $q\bar{q}$ events peaks towards ± 1 while it is flat for $B\bar{B}$ events.
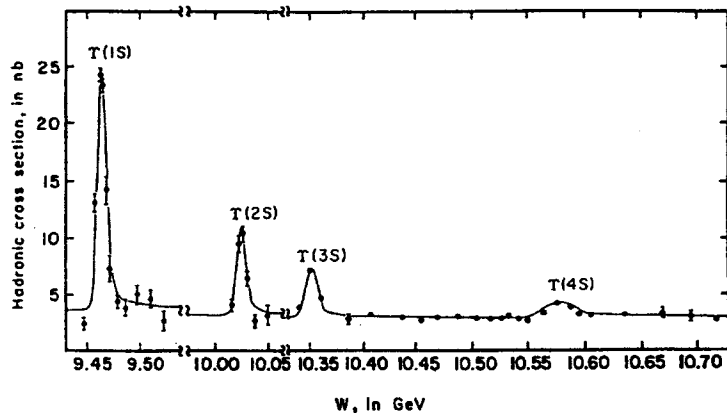
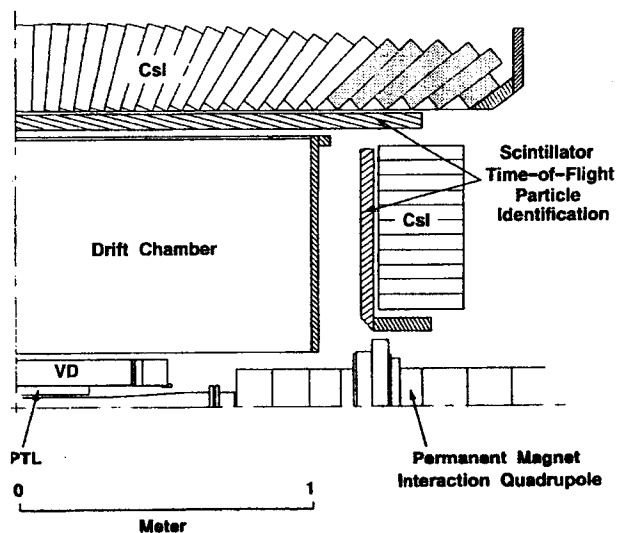Figure 1. Hadronic cross section as a function of center-of-mass energy, W.

Figure 2. Magnified view of the CLEO detector inside the magnetic coil.

In cases when it is possible to reconstruct one of the B mesons, there are two very powerful kinematic variables that are used. One, the difference between the candidate energy and the beam energy, ΔE, has a resolution between 17 MeV and 50 MeV, depending on decay mode. The second is the beam-constrained mass,

$$M_B = \sqrt{E_{beam}^2 - (\sum \vec{p})^2} \quad ,$$

(1)

where the sum is over the candidate tracks that are the selected decay products of the B meson. The resolution of M_B is about 2.5 MeV nearly independent of decay mode. It is dominated by the 2 MeV width of the beam. A B event will have ΔE close to 0 and M_B close to 5.280 GeV, the known mass of a B meson.

1.3 The CLEO Detector

The CLEO Detector is a 4π general-purpose detector utilizing a superconducting coil operating at 1.5 Tesla. All detection elements, except for the muon chambers, are inside the magnetic coil. Figure 2 shows a magnified view of those parts of the detector inside the coil.

Three drift chambers, the PTL, the VD, and the central Drift Chamber, provide up to 67 layers for tracking information. The momentum resolution obtained using these chambers is given by:

$$\left(\frac{\delta p}{p}\right)^2 = (0.005)^2 + (0.0015p)^2 \quad .$$

(2)

In addition, dE/dx is measured in the 51 layers of the central Drift Chamber with a resolution of 6.2% for electrons and 7.2% for hadrons.

The electromagnetic calorimeter is comprised of 7800 crystals of CsI and provides excellent energy resolution for photons and electrons. The resolution in the "good" barrel region is given by:

$$\frac{\delta E}{E}(\%) = 0.35/E^{0.75} + 1.9 - 0.1E \quad (E \text{ in GeV}) . \quad (3)$$

It is 2%, or better, for energies above 1 GeV.

1.4 The CKM Matrix

In the Standard Model, weak decays can be understood through the Cabibbo-Kobayashi-Maskawa (CKM) matrix which relates the physical quarks to their weak eigenstates.

$$V_{ij} = \begin{pmatrix} V_{ud} & V_{us} & V_{ub} \\ V_{cd} & V_{cs} & V_{cb} \\ V_{td} & V_{ts} & V_{tb} \end{pmatrix} . \quad (4)$$

The V_{ij} are not predicted by theory. They are fundamental parameters of the Standard Model and must be measured experimentally.

The elements V_{ub} and V_{cb} can be best measured in semileptonic decays of the B meson since there are no final state interactions between the lepton decay products of the W and the other final state quarks. In addition, V_{td} and V_{ts} can also be measured in B-meson decays either through box diagrams leading to mixing or single-loop penguin decays as indicated in Fig. 3.
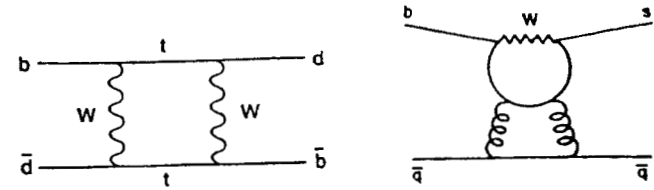

Figure 3. Feynman diagrams for B-meson decays: Box diagram for mixing and **penguin** diagram.

While there are several ways of representing the matrix elements, the Wolfenstein form, shown below, gives an indication as to the relative size of the elements.

$$V_{ij} = \begin{pmatrix} 1 - \lambda^2/2 & \lambda & A\lambda^3(\rho - i\eta) \\ -\lambda & 1 - \lambda^2/2 & A\lambda^2 \\ A\lambda^3(1 - \rho - i\eta) & -A\lambda^2 & 1 \end{pmatrix} . \quad (5)$$

The value of λ, the sine of the Cabibbo angle, is about 0.22 (Ref. 1). This also explicitly allows the possibility of CP violation in weak decays if η is not equal to zero.

2 Semileptonic Decays

2.1 Br(B→xlν) for B⁰ and B⁻; Three Different Tagging Methods

2.1.1 Fully Reconstructed B's

A total of 834 ± 42 B⁰ and 515 ± 31 B⁻ (and B+) mesons have been fully reconstructed as shown in Figs. 4(a) and 4(b). The fraction of these events that are accompanied by a lepton (e or μ) leads to the appropriate branching ratio. The results are
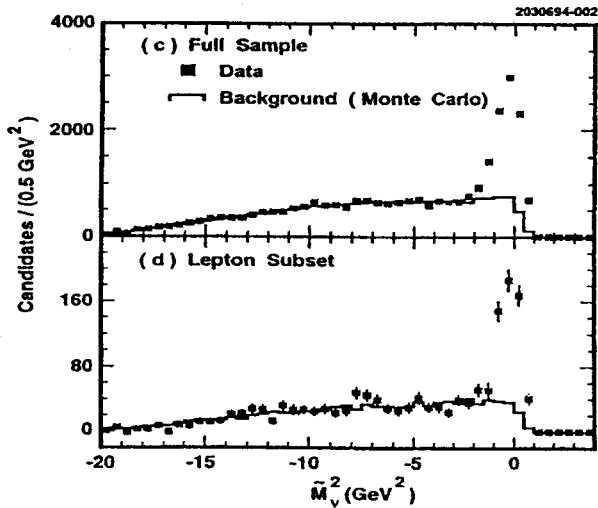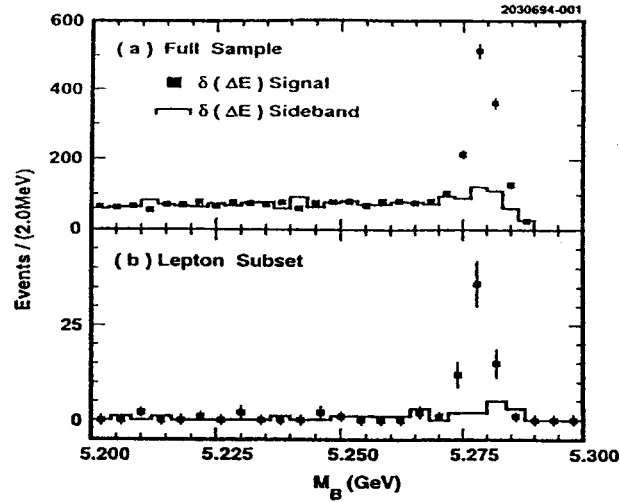
Figure 4. (a) Beam-constrained mass for fully reconstructed B mesons. The histogram is for events in the ΔE sideband. (b) is the same as (a) but for the lepton subset. (c) and (d) are similar to (a) and (b) for $\tilde{M}_\nu^2$ distribution.

$$b_0 \equiv \mathrm{Br}\left(B^0 \to Xl\nu\right) = (13.5 \pm 2.6)\%$$

$$b_- \equiv \mathrm{Br}\left(B^- \to Xl\nu\right) = (10.1 \pm 1.8)\% \ .$$

It should be noted that this is the first reported measurement for the charged B semileptonic branching fraction.

2.1.2 Partial Reconstruction of Semileptonic Decays

In order to increase the tagging efficiency compared to a full reconstruction, a partial reconstruction technique can be employed by taking advantage of the decay kinematics of the D^{*+} meson. Consider the tagging decay $\overline{B}^0 \to D^{*+}l^-\overline{\nu}$, where $D^{*+} \to D^0\pi^+$. The laboratory momentum of the π^+ varies around an average of about 0.2 GeV/c. Due to the low Q value of this decay, the energy, E_{D^*}, and momentum, $\overline{P}_{D^*}$ of the D^*, can be calculated by measuring the three-momenta of the π^+. In the approximation that the B is at rest, the missing neutrino mass can be written as

$$\tilde{M}_\nu^2 = \left(E_{beam} - E_{D^*} - E_l\right)^2 - \left(\overline{P}_{D^*} + \overline{P}_l\right)^2 . \tag{6}$$

Figures 4(c) and 4(d) show the distribution of $\tilde{M}_\nu^2$ for the full sample and for the lepton subset. The total number of B^0 decays in the signal region, $\tilde{M}_\nu^2 \geq -2\mathrm{GeV}^2$, for the full sample is 7119 ± 139. The resulting branching fraction is

$$b_0 = (10.5 \pm 0.8)\% .$$

2.1.3 Partial Reconstruction of Hadronic Decays

In the two-body tagging decay $\overline{B}^0 \to D^{*+}\pi^-$, the π^- has a momentum of 2.3 GeV/c. The D^{*+} energy and momentum can be reconstructed from the $D^0\pi^+$ decay as

described above. The D* can then be combined with the π^- to form a B candidate.[2]

With this technique, 822 ± 53 B^0 decays were reconstructed, leading to a branching fraction

$$b_0 = (10.2 \pm 1.9)\%.$$

2.1.4 Combining the Results

The weighted average for the three branching fractions for the B^0, including systematic errors, is

$$b_0 = (10.9 \pm 0.7 \pm 1.1)\%.$$

As given above, the branching fraction for the $\bar{B}^-$ is

$$b_- = (10.1 \pm 1.8 \pm 1.4)\%.$$

CLEO has also measured the charged average from the inclusive lepton spectra.[3] In that analysis, a fit must be made to the shape of both the primary $(b \rightarrow cl\nu)$ lepton spectrum and to the secondary cascade $(b \rightarrow c \rightarrow sl\nu)$ spectrum. These spectra depend on theory; hence the result is model dependent. Below are the two values for the two models considered.

$$\bar{b} = (10.98 \pm 0.10 \pm 0.33)\% \quad \text{IGSW}^4 \text{ with } 21\% \text{ D}^{**}$$

$$\bar{b} = (10.65 \pm 0.05 \pm 0.33)\% \quad \text{ACCMM}^5$$

We see that the average of the individual charged branching fractions agrees very well with either fit for $\bar{b}$, which is measured in an entirely independent manner.

In addition, since the ratio of the charged and neutral branching fractions is equal to the ratio of lifetimes, we have

$$b_- / b_0 = \tau_- / \tau_0 = 0.93 \pm 0.18 \pm 0.12.$$

This is very consistent with the newest world average, $\tau_- / \tau_0 = 1.003 \pm 0.069$, as reported in this conference by P. Wells.

2.2 B→Xeν with a Lepton Tag[6]

2.2.1 Br(B→Xeν)

When both B mesons decay semileptonically, we can take advantage of charge correlations and kinematics to get a model-independent measurement of $\bar{b}$, the charged average branching fraction.

A lepton (μ or e) with momentum greater than 1.4 GeV/c is the tag. The momentum cut ensures that there is very little contamination from b→c→s cascade leptons. If the other B decays semileptonically, its lepton will have an opposite charge to the tag lepton (neglecting mixing). In this analysis, only electrons are used for the "signal" lepton. Electrons can be identified down to a momentum of 0.6 GeV/c while muons are ranged out for momenta below 1.4 GeV/c. In order to reduce the model dependence, it is important to measure the "signal" lepton momentum to as low a value as possible.

The major background occurs when the charm system from the tag decay, $b \rightarrow cl_{tag}\nu$, also decays semileptonically. This lepton also has opposite charge relative to the tag. Since the B meson is produced almost at rest, the two leptons, in this case, will tend to be in opposite hemispheres. On the other hand, the leptons coming from opposite B's are uncorrelated. Figure 5 shows a Monte Carlo generated scatter plot of the electron momentum versus the cosine of the angle between the electron and lepton tag. A diagonal cut, $p_{e-} + \cos(l,e) > 1$, is made which reduces this background by a factor of 25 and maintains 67% of the signal.

After the cut, there are a total of $245,255 \pm 76$ lepton tags. Figure 6 shows the resulting electron momentum spectrum. The solid curve shows the shape due to the ACCMM theory. It is shown only to indicate what fraction of the signal must be extrapolated from theory. This fraction is $(5.8 \pm 0.5)\%$, where the uncertainty is due
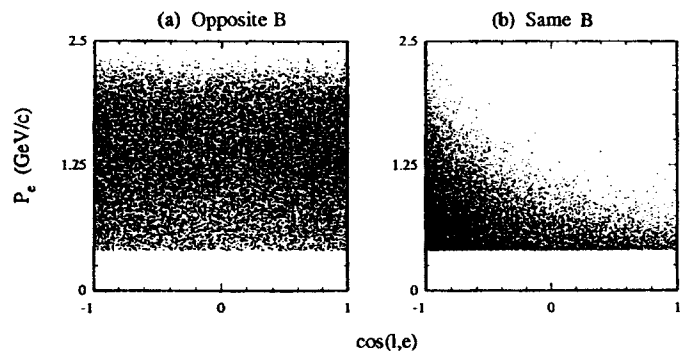
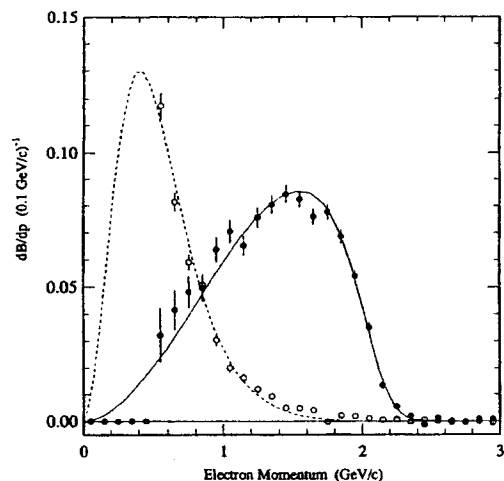Figure 5. Distribution of electrons from (a) opposite B and (b) same B.

Figure 6. Spectrum of primary electrons (dots), and that of the secondary electrons (open circles).

to the range of the different models. The resulting branching fraction is

$$\overline{b} = Br(B \to Xe\nu) = (10.36 \pm 0.17 \pm 0.40)\% .$$

The systematic (second) error is dominated by the estimate in the fake electron rate. There is a very small contribution due to any model dependence.

2.2.2 Br(Υ(4s)→non-BB̄)

The above result depends on the number of lepton tags, not on the number of $B\overline{B}$ pairs produced on the $\Upsilon(4s)$. Using this fact, we can obtain a measurement of the branching fraction for the $\Upsilon(4s)$ to decay to non-$B\overline{B}$ states. Almost all B–meson branching fractions measured on the $\Upsilon(4s)$ are calculated assuming this number is zero. The number of electrons per unit momentum interval can be written in terms of the number of $\Upsilon(4s)$ events and the electron spectrum $\dfrac{dB}{dp}$ as

$$\frac{dN(e^{\pm})}{dp} = 2N_{\Upsilon(4s)}(1-f)\eta(p)\frac{dB}{dp} , \qquad (7)$$

where f is the fraction of non–$B\overline{B}$ decays, and $\eta(p)$ is the momentum–dependent efficiency. Integrating this over the entire sample ($p \geq 0.6$ GeV/c) gives

$$f = 0.010 \pm 0.014 \pm 0.011 .$$

This is an especially important result. It can be stated with reasonable certainty that the experimentally measured semileptonic branching fraction is less than 11%. On the other hand, theory predicts a value that should be no less than 12.5% (Ref. 7). If the non-BB branching fraction were of the order of 15%, it would bring theory and experiment into agreement. But the above measured fraction implies a 95% confidence level upper limit of 0.04. The difference between theory and experiment cannot be explained by production of non–$B\overline{B}$ states at the $\Upsilon(4s)$.

2.3 B→D*lν

2.3.1 Br(B→D*lν)

As noted above, when the B decays to a D^*, the slow π from the decay of the D^* provides a very clear experimental signature. In addition, the recent development of Heavy Quark Effective Theory (HQET)[8] allows a measurement of $|V_{cb}|$ from $B \to D^*l\nu$ that has a smaller model dependence than previous determinations.

CLEO has made a new measurement of the branching fractions for the decays $\overline{B}^0 \to D^{*+}l^-\overline{\nu}$ and $B^- \to D^{*0}l^-\overline{\nu}$. The basic method is to combine a fully reconstructed D^* with the correct sign lepton (e or μ) in the event. D^* mesons are reconstructed using the decay chains $D^{*+} \to D^0\pi^+$, $D^{*0} \to D^0\pi^0$, and $D^0 \to K^-\pi^+$. An effective constraint is obtained by insisting that the kinematics of the candidate decay be consistent with a neutrino being the only missing particle.

The D^* meson is reconstructed by fitting the D^0 mass peak after making a cut on the D^*-D^0 mass difference, $\delta_m \equiv M_{K\pi\pi} - M_{K\pi}$, and subtracting any fit D^0's in a δ_m sideband. The δ_m signal region for D^{*+} is 8 MeV wide and is centered on 145.44 MeV while for the D^{*0}, it is 6 MeV wide centered on 142.12 MeV. Figure 7 shows the δ_m distribution for D^{*+} and D^{*0} events which have $M_{K\pi}$ within 100 MeV of the measured D^0 mass. The $M_{K\pi}$ distributions for events in the δ_m signal and sideband regions are shown in Fig. 8.

The resulting yield for the $\overline{B}^0$ decay is $376 \pm 27 \pm 16$, while for the B^- mode, the yield is $302 \pm 32 \pm 13$. Under the assumption that the fraction of produced neutral B mesons (f_{00}) is equal to the fraction of charged B mesons (f_{+-}), we get the following branching fractions:

$$Br\left(\overline{B}^0 \to D^{*+}l^-\overline{\nu}\right) = [4.49 \pm 0.32 \pm 0.39]\%$$

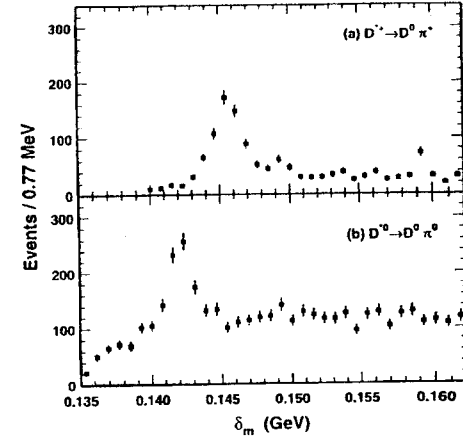$$Br\left(B^- \to D^{*0}l^-\overline{\nu}\right) = [5.13 \pm 0.54 \pm 0.64]\% \ .$$

Figure 7. Mass difference, δ_m, distribution for events falling within the signal kinematic boundary for (a) $\overline{B}^0 \to D^{*+}l^-\overline{\nu}$, and (b) $B^- \to D^{*0}l^-\overline{\nu}$. All candidates are required to have $M_{K\pi}$ within 100 MeV of the measured D^0 mass.
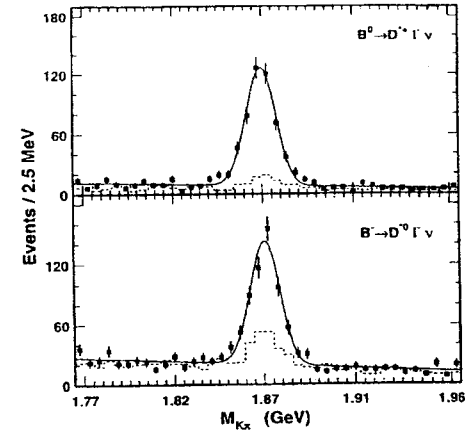
Figure 8. Invariant mass of $K^-\pi^+$ combinations passing the δ_m cut. The dashed histograms show the scaled $M_{K\pi}$ distributions for the δ_m sideband.

2.3.2 f_{+-}/f_{00}

If we do not make the assumption that $f_{00} = f_{+-}$, but instead assume only that

$$\Gamma\left(\overline{B}^0 \to D^{*+}l^-\bar{\nu}\right) = \Gamma\left(B^- \to D^{*0}l^-\bar{\nu}\right), \qquad (8)$$

we can obtain a value for f_{+-}/f_{00}. We can write for the neutral and charged yields

$$N_0 = 4N_{\Upsilon(4s)}f_{00}Br\left(\overline{B}^0 \to D^{*+}l^-\bar{\nu}\right)B_{D^{*+}}B_{D^0}, \qquad (9)$$

$$N_- = 4N_{\Upsilon(4s)}f_{+-}Br\left(\overline{B}^- \to D^{*0}l^-\bar{\nu}\right)B_{D^{*0}}B_{D^0}, \qquad (10)$$

where
$$B_{D^{*+}} = Br\left(D^{*+} \to D^0\pi^+\right) = (68.0 \pm 1.0 \pm 1.3)\%,$$

and
$$B_{D^{*0}} = Br\left(D^{*0} \to D^0\pi^0\right) = (63.6 \pm 2.3 \pm 3.3)\% \text{ [Ref. 9]}.$$

Dividing the second equation by the first, we get

$$\frac{f_{+-}}{f_{00}}\frac{\tau_{B^-}}{\tau_{B^0}} = \frac{N_-}{N_0}\frac{B_{D^{*+}}}{B_{D^{*0}}} = 1.14 \pm 0.14 \pm 0.13$$

Using the value of $\tau_{B^-}/\tau_{B^0} = 1.10 \pm 0.11$ (Ref. 10), we get

$$\frac{f_{+-}}{f_{00}} = 1.04 \pm 0.13 \pm 0.12 \pm 0.10.$$

The third error is due to an uncertainty in the lifetime ratios.

2.3.3 $|V_{cb}|$ via HQET

Generally, the amplitude for $B \to D^*l\nu$ depends on three independent form factors which are functions of q^2, the mass of the virtual W. But, in HQET, in the limit of infinite b and c quark masses, the three form factors are given in terms of a single form factor $\xi(y)$, known as the Isgur-Wise function. The variable y is given by

$$y = v \cdot v' = \left(M_B^2 + M_{D^*}^2 - q^2\right)/\left(2M_B M_{D^*}\right), \qquad (11)$$

where v and v' are the four velocities of the B and D^* mesons, and M_B and M_{D^*} are their respective masses. At y=1 (maximum q^2), $\xi(1)$ is normalized to unity. For finite quark masses, the differential decay rate can still be expressed in terms of a single unknown form factor F(y). F(1) can be calculated in perturbative QCD to have the value $0.93 \pm .04$ (Refs. 11 and 12).

The differential decay rate can be written as

$$\frac{d\Gamma}{dy} = G(y)|V_{cb}|^2 F^2(y), \qquad (12)$$

where G(y) is a known function which has the property that it is zero at y=1. Thus, $\frac{d\Gamma}{dy}$ must be extrapolated to y=1 in order to obtain $|V_{cb}|$. Since the shape of F(y) is unknown, results from both a linear and quadratic fit are obtained.

Figure 9 shows $|V_{cb}|F(y)$ vs. y with both fits. The more precise value comes from the linear fit which gives

$$|V_{cb}| = 0.0377 \pm 0.0019 \pm 0.0020 \pm 0.0014,$$

where the third error is due to the uncertainty in F(1) and the lifetime uncertainty has been included in the second (systematic) error.
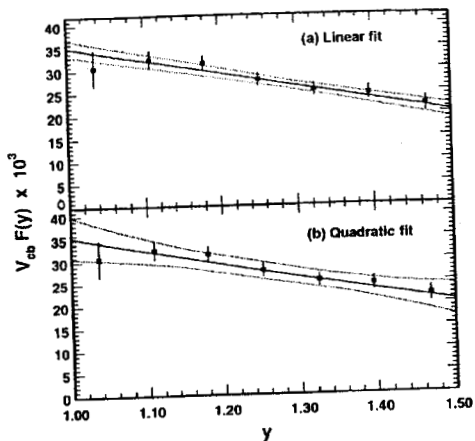
Figure 9. The product $|V_{cb}|F(y)$ (solid line) as determined by fits to the combined $D^{*+}l^-$ and $D^{*0}l^-$ data using (a) a linear expansion and (b) a quadratic expansion for the form factor $F(y)$. The dotted lines show the contours for 1σ variations of the fit parameters.

3. Two-Body Nonleptonic Decays

3.1 Factorization

The semileptonic decay of B^0 to a D^{*+} must occur via the external spectator diagram shown in Fig. 10(a). The amplitude for this decay factorizes into a product of leptonic and hadronic currents since leptons do not interact through the strong interaction. Figure 10(a) also shows the corresponding hadronic decay diagram. The factorization hypothesis states that the amplitude for this decay can be expressed theoretically as the product of two hadronic currents, one describing the formation of the D^{*+} meson and the other the hadronization of the $\bar{u}d$ system from the virtual W^-. In other words, the D^{*+} is "unaware" of whether the W^- decayed into leptons or

hadrons. Most theories of two-body hadronic decays of the B meson are based on the factorization hypothesis.
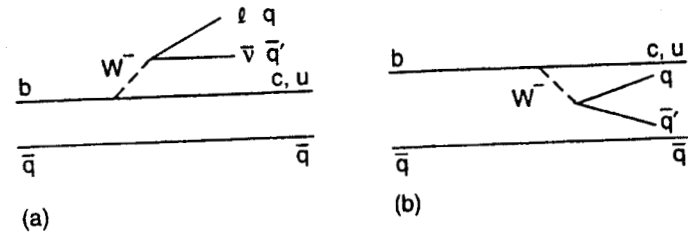

Figure 10. B–meson decay spectator diagrams. (a) External semileptonic or hadronic decay and (b) color suppressed, internal spectator decay.

Factorization can be tested experimentally by verifying the relation

$$\frac{\Gamma(\bar{B}^0 \to D^{*+}h^-)}{\dfrac{d\Gamma}{dq^2}(\bar{B}^0 \to D^{*+}l^-\nu)\bigg|_{q^2=m_h^2}} = 6\pi a_1^2 f_h^2 |V_{ud}|^2 . \quad (13)$$

The condition $q^2 = m_h^2$ (q^2 is the mass of the lepton-neutrino system which is the mass of the virtual W^-) ensures that the kinematics of the leptonic system is the same as the hadronic system. The factor $a_1 = 1.1 \pm 0$ is due to a hard gluon QCD correction, and f_h is the appropriate decay constant for the hadron h. CLEO has data for the cases when $h=\pi$, ρ and a_1 as shown in Fig. 11. In addition, both CLEO and ARGUS have measurements for $d\Gamma/dq^2$ as a function of q^2. These are shown in Figure 11(d) along with several theoretical fits to the data. From these data, we can form the left-hand ratio in Eq. (13) which we denote as R_{exp}. For the right-hand side, R_{Theo}, we use the measured value $f\pi = 131.7 \pm 0.15$ MeV, $f\rho = 215 \pm 4$ MeV, and $f_{a_1} = 205 \pm 16$ MeV.
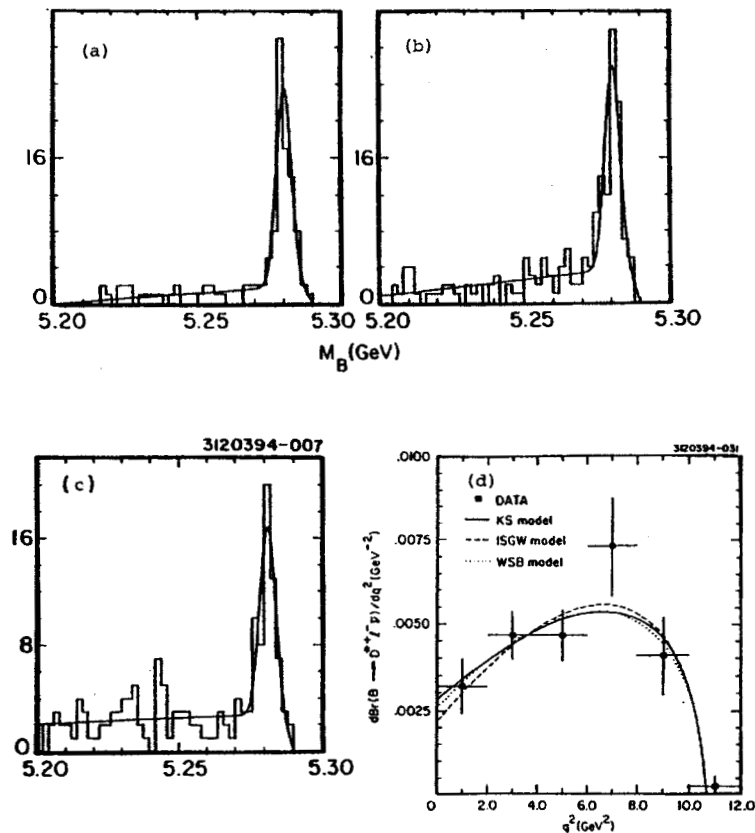
Figure 11. M_B distribution for (a) $\overline{B}^0 \to D^{*+}\pi^-$, (b) $\overline{B}^0 \to D^{*+}\rho^-$, (c) $\overline{B}^0 \to D^{*+}a_1^-$, and (d) q^2 distribution for the decay $\overline{B}^0 \to D^{*+}l^-\overline{\nu}$. The points are a weighted average from CLEO and ARGUS data.

The comparison for the three decay modes are shown below:

Mode	$R_{exp}(\text{Gev}^2)$	$R_{Theo}(\text{Gev}^2)$
$D^{*+}\pi^-$	$1.1 \pm 0.1 \pm 0.2$	1.2 ± 0.2
$D^{*+}\rho^-$	$3.0 \pm 0.4 \pm 0.6$	3.3 ± 0.5
$D^{*+}a_1^-$	$4.0 \pm 0.6 \pm 0.5$	3.0 ± 0.5 .

It seems, for hadronic masses up to the a_1, the factorization hypothesis is valid.

3.2 External Spectator vs. Color-Suppressed Decays

In the BSW model,[13] external spectator decays as depicted in Fig. 10(a) should have branching ratios dependent on an amplitude denoted as a_1. On the other hand, internal spectator decays, as shown in Fig. 10(b), should depend on a much smaller amplitude, a_2, due to the fact that the colors of the quarks from the W^- decay must match the colors of the c quark and accompanying spectator quark.

$\overline{B}^0$ decays to $D^+\pi^-$, $D^+\rho^-$, $D^{*+}\pi^-$, and $D^{*+}\rho^-$ are purely external modes. Their branching fractions are proportional to a_1^2. The mass distribution for the first two modes is shown in Figs. 12(c) and 12(d). The second two modes were discussed in the previous section. A fit to the branching fractions yields $|a_1| = 1.15 \pm 0.04 \pm 0.05 \pm 0.09$.

Modes with ψ mesons in the final state are due to pure internal decays. Figure 13 shows four of these modes. From these, we get $|a_2| = 0.26 \pm 0.01 \pm 0.01 \pm 0.02$. The second systematic error on $|a_1|$ and $|a_2|$ is due to the uncertainties due to the B-meson production fractions and lifetimes (i.e., $f_{+-}\tau_+/f_{00}\tau_0$).
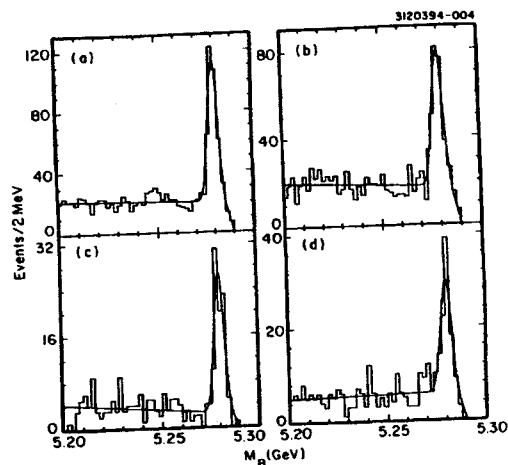
Figure 12. M_B distribution for (a) $B^- \to D^0\pi^-$, (b) $B^- \to D^0\rho^-$, (c) $\overline{B}^0 \to D^+\pi^-$, and (d) $\overline{B}^0 \to D^+\rho^-$.
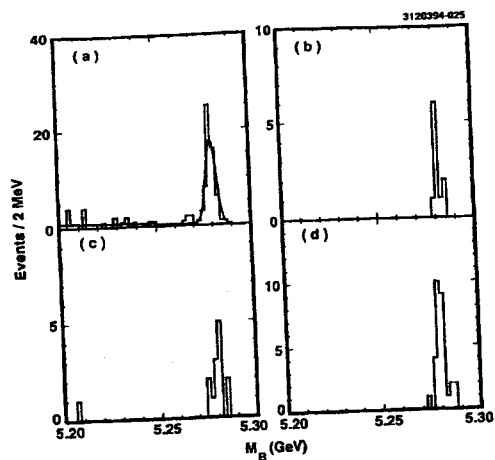

Figure 13. Beam constrained mass for (a) $B^- \to \psi K^-$, (b) $\overline{B}^0 \to \psi \overline{K}^0$, (c) $B^- \to \psi K^{*-}$, and (d) $\overline{B}^0 \to \psi K^{*0}$.

The sign of a_2 relative to a_1 can be determined by comparing charged and neutral modes. The BSW model predicts the following four ratios:

$$R_1 = Br(B^- \to D^0\pi^-)/Br(\overline{B}^0 \to D^+\pi^-) = (1+1.23\,a_2/a_1)^2$$
$$R_2 = Br(B^- \to D^0\rho^-)/Br(\overline{B}^0 \to D^+\rho^-) = (1+0.66\,a_2/a_1)^2$$
$$R_3 = Br(\overline{B} \to D^{*0}\pi^-)/Br(\overline{B}^0 \to D^{*+}\pi^-) = (1+1.29\,a_2/a_1)^2$$
$$R_4 = Br(B^- \to D^{*0}\rho^-)/Br(\overline{B}^0 \to D^{*+}\rho^-) = (1+0.75\,a_2/a_1)^2 .$$

The charge modes can occur through either an external or internal decay, and thus depend on a sum of a_1 and a_2 amplitudes. Figures 12(a) and 12(b) show the data for the two D^0 charged B modes.

Table 1 shows the model predictions for the two a_2/a_1 ratios and the experimental results.

TABLE 1. Ratios of normalization modes to determine the sign of a_2/a_1. The magnitude of a_2/a_1 is the value in the BSW model which agrees with the results from the $B \to \psi$ modes.

Ratio	$a_2/a_1 = -0.24$	$a_2/a_1 = 0.24$	CLEO II
R_1	0.50	1.68	$1.89 \pm 0.26 \pm 0.32$
R_2	0.71	1.34	$1.67 \pm 0.27 \pm 0.30$
R_3	0.48	1.72	$2.00 \pm 0.37 \pm 0.28$
R_4	0.41	1.85	$2.27 \pm 0.41 \pm 0.41$

4 Rare Decays

4.1 Introduction

In this paper, rare decays refer to spectator b→u decays or penguin decays (one-loop flavor changing neutral current diagrams). Penguin diagrams were originally introduced to explain the $\Delta I = \frac{1}{2}$ rule in K decays. They are possible candidates for direct CP violation. In B decays, the penguin branching fractions are expected to be several orders of magnitude larger than for the corresponding K decays. In addition, they could provide a window on new physics in that the existence of new particles (e.g., charged Higgs) could affect the overall amplitude for the decay.

Figure 14(a) shows the pure penguin diagram for $B^0 \to \phi K^0$ while Figs. 14(b) and 14(c) show both the penguin and b → u spectactor diagrams for $B^0 \to K^+\pi^-$. Interference between these latter two diagrams could lead to CP violation.

(a)   (b)

(c)
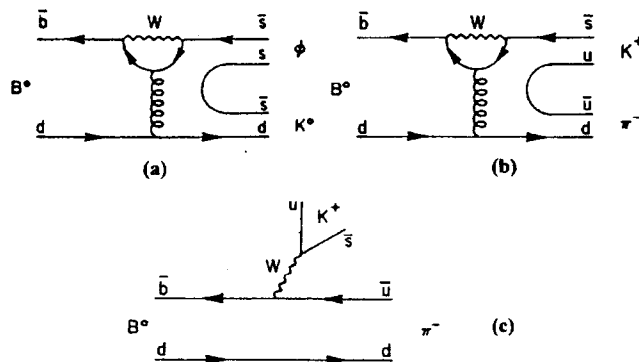
Figure 14. (a) Penguin diagram for $B^0 \to \phi K^0$. (b) Penguin diagram for $B^0 \to K^+\pi^-$. (c) Spectator diagram for $B^0 \to K^+\pi^-$. The spectator decay is doubly suppressed since $\Gamma \alpha |V_{ub}V_{us}|^2$.

Decays such as $B^0 \to \pi^+\pi^-$ and $B^0 \to \pi^+\rho^-$ should be dominated by the b→u spectator diagram. Measurements of their branching fractions can be used to extract a value for $|V_{ub}|$. Also, the mode $B^0 \to \pi^+\pi^-$ can be used to measure CP violation since the $\pi^+\pi^-$ final state is a CP eigenstate. CP violation can arise from the interference between the amplitude for direct decay and the amplitude when the B^0 mixes into a $\overline{B}^0$ and then decays.

4.2 Charmless Hadronic Decays

CLEO has done an extensive search for two-body charmless hadronic rare decays. The results quoted here are based on an integrated luminosity on the $\Upsilon(4s)$ of 2.0 fb^{-1} (2.2×10^6 produced $B\overline{B}$ pairs) and 0.9 fb^{-1} on the continuum just below the $\Upsilon(4s)$.

The major challenge for the analysis in all these modes is continuum suppression. This is accomplished by the use of four variables. One is $\cos\theta_t$ which was discussed in Sec. 1. Another is the Fisher Discriminant, F. It is a single variable formed by a linear combination of N (for this analysis N=11) variables defined as

$$F = \sum_{i=1}^{N} \alpha_i x_i \ . \tag{14}$$

The x_i are the set of the N individual variables, each of which usually gives relatively weak discrimination between signal and background. The α_i are chosen by the use of Monte Carlo to optimize the difference between signal and background. The single variable, F, gives enhanced discrimination power. The sum of chi-squares and neural networks are examples of other techniques that combine multiple variables into a single number. Figure 15 shows the Fisher Discriminant for both signal and continuum background. The distributions are close to Gaussian in shape with about one sigma

separation. A cut of F < 0.5 keeps 80% of the signal while rejecting 50% to 70% of the background, depending on the mode.
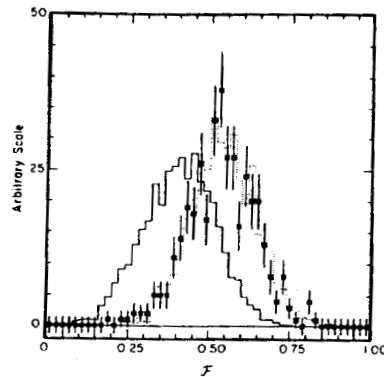

Figure 15. Fisher Discriminant distribution. The solid histogram is for a Monte Carlo generated signal. The points are for continuum data and the dotted histogram is for Monte Carlo generated continuum.

The other two variables are ΔE, the difference between the energy of the B-meson candidate and the beam energy, and M_B, the beam–constrained mass. In order to enhance the statistics on the background, we look at a relatively large region in the $\Delta E - M_B$ plane. This is shown in Fig. 16 for the data $B^0 \to K^+\pi^-$. The signal region is defined as covering $\pm 2\sigma$. For ΔE, σ varies from 17 MeV to 50 MeV, depending on mode. The ratio of the area of the entire sideband region to the area of the signal region is about 30. The error on the background determination is improved by the square root of this ratio compared to the error that is obtained by taking the sideband region as the same size as the signal region.
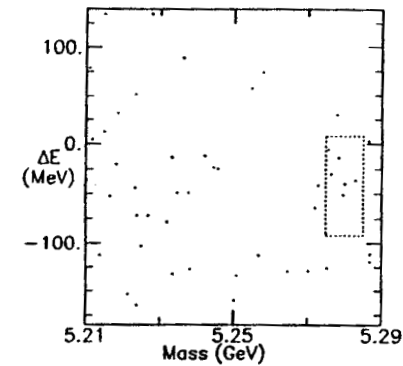

Figure 16. Scatter plot in the $\Delta E - M_B$ plane for data that passes the $\cos\theta_t$ and Fisher cuts, and satisfies the hypothesis $B^0 \to K^+\pi^-$.

In our analysis of $B^0 \to \pi^+\pi^-$ and $B^0 \to K^+\pi^-$, we have used dE/dx and the energy difference between the K and π to help distinguish between these two modes. At 2.6 GeV, the dE/dx separation between the π and K is 1.8σ. The energy difference is 42 MeV which corresponds to 1.7σ. We have combined these with the three variables F, ΔE, and M_B to do a likelihood fit to extract the yields in each mode. These results have already been published,[14] but the new fit shown in Fig. 17 includes 50% more data. Table 2 gives the updated results. Since the signal for either individual mode is less than 3σ, we quote upper limits only. On the other hand, the combined result has a significance of 5.3σ statistical and 4.0σ when systematics are included.

All other rare modes that we have measured so far are shown in Table 3. No signal has been observed for any of these modes so 90% confidence level upper limits are given. In all cases, these limits are below those previously published. In some, there
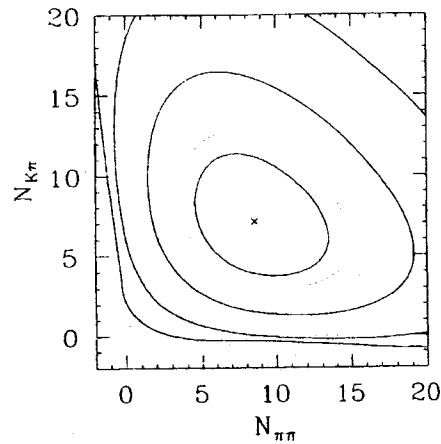
Figure 17. Maximum likelihood fit for $B^0 \to \pi^+\pi^-/K^+\pi^-$. The solid curves show the 1, 2, 3, and 4 sigma contours. The dotted curve is the 1.28 sigma contour.

TABLE 2. Updated results for $B^0 \to K^+\pi^-$, $\pi^+\pi^-$, and K^+K^-. Upper limits are at the 90% confidence level.

Mode	Event Yield	BR(10^{-5})	Theoretical Predictions[15] (10^{-5})
$\pi^+\pi^-$	$8.5^{+4.9}_{-4.0}$	< 2.2	1.0-2.6
$K^+\pi^-$	$7.1^{+4.2}_{-3.4}$	< 1.9	1.0-2.0
K^+K^-	$0.0^{+1.6}_{-0.0}$	< 0.7	—
$\pi^+\pi^- + K^+\pi^-$	$5.7^{+5.3}_{-4.5}$	$1.8^{+0.6}_{-0.5} \pm 0.2$	

TABLE 3. Event yields, estimated background in the signal region, upper limits on the branching ratios, previous upper limits, and theoretical predictions. Upper limits are at the 90% confidence level. For the decays $B \to X_s\phi$, particles in parentheses indicate a $K^*(892)$ decaying to those particles.

Mode	Event Yield	Est. Bkgr.	Upper Limit on BR (10^{-5})	Previous UL (10^{-5})	Theory (10^{-5})
$\pi^0\pi^0$	1	1.7 ± 0.4	1.0	–	0.03-0.10
$\pi^\pm\rho^\mp$	6	2.4 ± 0.6	9.5	52	1.9-8.8
$\pi^0\rho^0$	1	1.5 ± 0.5	2.9	40	0.07-0.23
$\pi^+\pi^0$	8	5.8 ± 0.6	2.3	24	0.6-2.1
$\pi^+\rho^0$	3	1.8 ± 0.3	4.1	15	0.0-1.4
$K^0\pi^0$	2		6.3	–	0.5-0.8
$K^{*+}\pi^-$	3	0.6 ± 0.2	23.8	44	0.1-1.9
$K^{*0}\pi^0$	0	0.9 ± 0.3	3.5	–	0.3-0.5
$K^+\rho^-$	2	1.7 ± 0.4	4.3	–	0.0-0.2
$K^0\phi$	1		10.7	49	0.1-1.3
$(K^+\pi^-)\phi$	1				
$(K^0\pi^0)\phi$	0				
$K^{*0}\phi$ (combined)	1		3.9	32	0.0-3.1
$\phi\phi$	0		4.8	–	–
$K^+\pi^0$	10	5.0 ± 0.5	3.2	–	0.3-1.3
$K^0\pi^+$	6	2.0 ± 0.5	6.8	9	1.1-1.2
$K^{*0}\pi^+$	2	0.6 ± 0.2	6.0	13	0.6-0.9
$K^+\rho^0$	1	1.1 ± 0.2	2.6	7	0.01-0.06
$K^+\phi$	0		1.4	8	0.1-1.5
$(K^+\pi^0)\phi$	0				
$(K^0\pi^+)\phi$	1				
$K^{*+}\phi$ (combined)	1		9.0	130	0.0-3.1

has been an improvement by an order of magnitude or more. In several cases (e.g., $B^0 \to \pi^{\pm}\rho^{\mp}$, $B^+ \to \pi^+\pi^0$), the upper limits are comparable to some of the theoretical predictions. Figure 18 shows the M_B distribution for the ϕ modes, which are particularly free of background.

4.3 Measurement of Inclusive $b \to s\gamma$

Last year, CLEO established the existence of the penguin process $b \to s\gamma$ by observing the decay $B \to K^*(892)\gamma$ (Ref. 16). The theoretical prediction of this exclusive rate has a large model dependence. On the other hand, the inclusive rate can be calculated within the framework of the Standard Model.[17] The largest theoretical uncertainties stem from the choice of renormalization scale μ and the fact that not all of the next-to-leading logarithmic QCD corrections have been calculated.[18] When these corrections have been completed, then the measurement of the inclusive rate can place stringent limits on a wide variety of nonstandard models as indicated in the list below taken from Joanne Hewett's talk given at the 1993 Summer Institute.[19]

"Top Ten" Models Constrained by $b \to s\gamma$:

1. Standard Model
2. Anomalous Top-Quark Couplings
3. Anomalous Trilinear Gauge Couplings
4. Fourth Generation
5. Two-Higgs-Doublet Models

6. Supersymmetry
7. Three-Higgs-Doublet Model
8. Extended Technicolor
9. Leptoquarks
10. Left-Right Symmetric Models

This year, CLEO has measured the inclusive branching fraction for $b \to s\gamma$. The signature is a photon with an energy between 2.2 and 2.7 GeV. Most models indicate that 75-90% of the photons from the $b \to s\gamma$ process lie in this range. The background
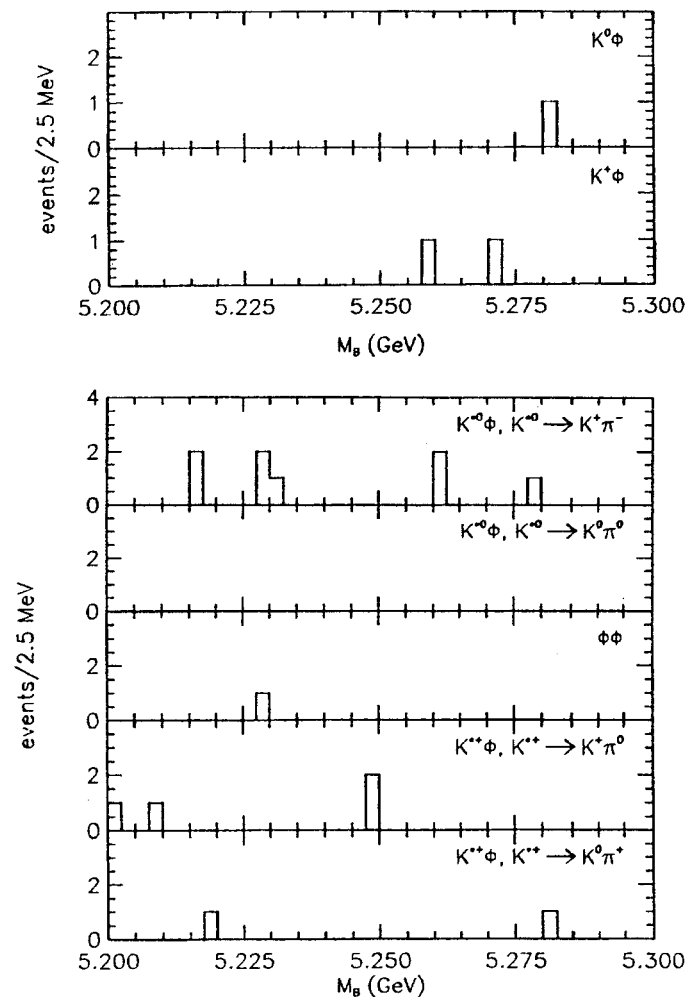

Figure 18. Beam constrained mass for $B \to \phi X$ where X is as indicated.

from other B decays is small and can be calculated. However, the background of photons from the continuum is large and complicated by the fact that there are two different processes contributing: $e^+e^- \rightarrow q\bar{q}$ with photons coming primarily from unvetoed π^0 and η decays, and initial state radiation (ISR) where $e^+e^- \rightarrow q\bar{q}\gamma$. Two different techniques have been developed to suppress these backgrounds.

4.3.1 Continuum Suppression with a Neural Network

In the neural network, as in the Fisher Discriminant, we form a single variable from a combination of event-shape variables. The eight variables we have used are described below and their distributions are shown in Figs. 19 and 20.

- R_2. This is the second Fox-Wolfram moment already described in Sec. 1.2.

- $S_\perp$. This variable takes advantage of the fact that the high-energy photon gives the event an axis. It is defined as

$$S_\perp = \frac{\displaystyle\sum_{\theta > 45^\circ} p_\perp}{\displaystyle\sum_{all} p} \qquad (\theta = \text{angle with respect to the } \gamma) . \qquad (15)$$

It discriminates most against $q\bar{q}$-continuum events.

- R'_2. This is the R_2 variable but calculated in the rest frame of the e^+e^- after the radiation of the high-energy photon (the primed frame). It discriminates most against ISR events.

- $\cos\theta'$. θ' is the angle between the photon and the thrust axis of the rest of the event in the primed frame. Again, it tends to discriminate against ISR events.

- Energy cones. There are four energy-flow cones centered on the high–energy photon. The distributions for the three different types of events are shown in Fig. 20.
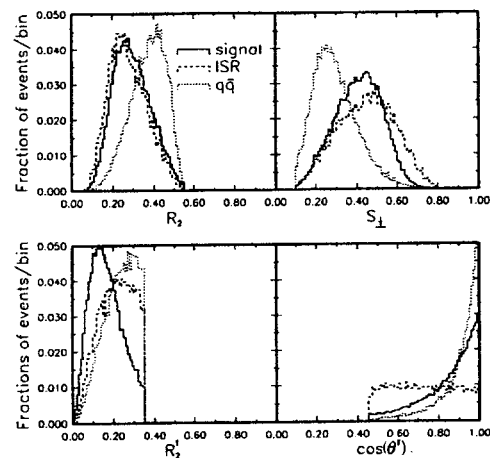

Figure 19. R_2, $S_\perp$, R'_2, $\cos(\theta')$ distributions for simulations of signal (solid), ISR (dashed), and $q\bar{q}$ (dotted).
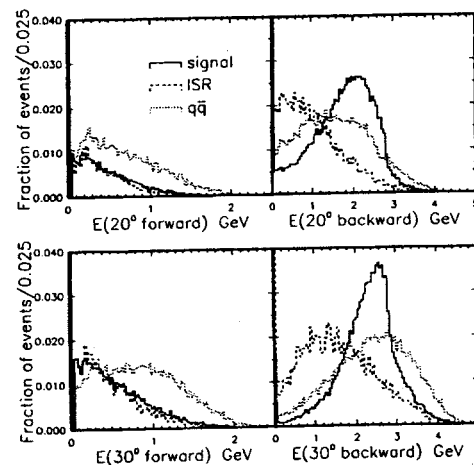

Figure 20. Distributions of energy cone variables for simulations of signal (solid), ISR (dashed), and $q\bar{q}$ (dotted).

The single neural network output, r, formed from these eight variables is shown in Fig. 21. It varies from -1 to +1. As can be seen, it gives good discrimination between signal and background.
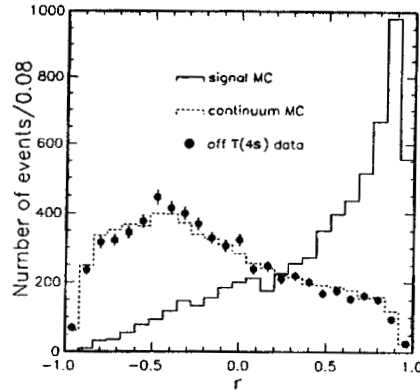

Figure 21. Distribution of single neural network output variable, r, for simulations of signal (solid) and background (dashed). The points are for off-resonance data.

4.3.2 Continuum Suppression Using Inclusive B Reconstruction

The basic approach is to look for one or more combinations of particles that fits the $B \rightarrow X_s \gamma$ decay hypothesis. X_s includes a $K^\pm$ or K^0 with up to four pions which may include at most one π^0. This technique provides continuum suppression but does not necessarily give the correct decay mode. $K^\pm$ and $\pi^\pm$ candidates are required to have a measured dE/dx within $\pm 3\sigma$ for that mass hypothesis. The $K^\pm$ cut is tightened to 2.5σ after the best track combination is selected. A K_s^0 is reconstructed from $\pi^+ \pi^-$ pairs with a displaced vertex with a mass within 3σ of the accepted K_s^0 mass.

For each candidate combination, the total energy and momentum is formed from the sum of the individual particle energies and vector momenta, respectively. The

energy difference, ΔE, and beam-constrained mass, M_B, as described in Sec. 1.2 are calculated. From M_B, the mass difference $\Delta M = (M_B - 5.279)$ GeV is calculated. Finally, a χ^2 variable χ_B^2 is formed:

$$\chi_B^2 = (\Delta M / \sigma_M)^2 + (\Delta E / \sigma_E)^2. \tag{16}$$

If there is more than one candidate combination in an event, the one with the lowest value of χ_B^2 is chosen. Thus, there is only one allowed combination per event. The distributions of χ_B^2 for the signal, the $q\bar{q}$, and the ISR backgrounds are shown in Fig. 22. To be accepted, an event must have χ_B^2 less than six.
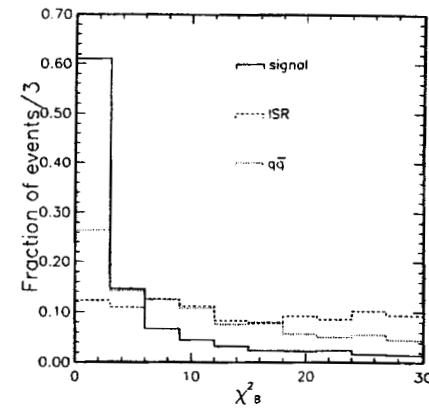

Figure 22. The χ_B^2 distribution for simulations of the signal (solid), the $q\bar{q}$ (dotted), and ISR (dashed) backgrounds.

4.3.3 Results

The photon energy spectrum as obtained from the neural network analysis is shown in Fig. 23(a). The solid histogram is the on-resonance data. The dotted histogram represents the scaled off-resonance data while the points represent the off-resonance
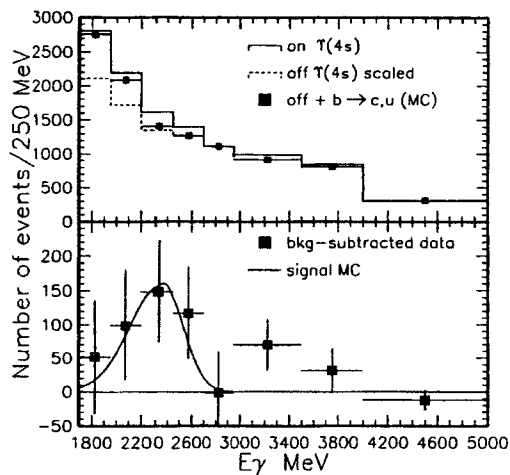
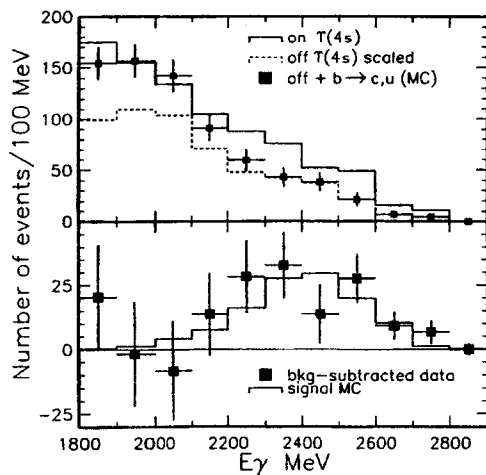Figure 23. Photon energy distribution from the neural network analysis.

Figure 24. Photon energy distribution from the B-reconstruction analysis.

data plus the expected $\Upsilon(4s)$ background. Figure 23(b) shows the background-subtracted data. Figure 24 shows the corresponding distributions for the B-reconstruction analysis.

Since the B-reconstruction technique selects a best X_S candidate, we can plot an apparent X_S mass distribution. This is shown in Fig. 25. While the spectrum should not be taken too literally, the peak at low mass seems to be clear evidence for $B \rightarrow K^*(892)\gamma$. The derived rate is consistent with our previously published result.[16]
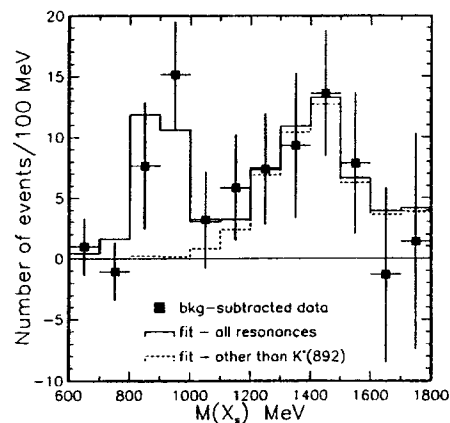

Figure 25. X_S mass distribution from the B-reconstruction analysis.

Table 4 summarizes the yields for both techniques. The detection efficiency is 0.38 for the neural network analysis and 0.104 for the B-reconstruction analysis. The fraction of photons from the $b \rightarrow s\gamma$ decay between 2.2 and 2.7 GeV is 0.85 (Ref. 20).

Combining the yields and efficiencies with the number of produced $B\bar{B}$ events of 2.15×10^6 gives the branching fractions $Br(b \rightarrow s\gamma) = (1.88 \pm 0.67) \times 10^{-4}$ and $(2.76 \pm 0.63) \times 10^{-4}$ for the neural network and B-reconstruction analyses, respectively. We have determined that the two methods have a slight degree of

correlation. The statistical error on the combined result is only 12% larger than the error would be if the two analyses were uncorrelated. The combined results, including systematic errors, is

$$Br(b \to s\gamma) = (2.32 \pm 0.51 \pm 0.29 \pm 0.32) \times 10^{-4}.$$

The first error is statistical, the second is systematic due to the uncertainty in yield, and the third is the systematic error due to the uncertainty in efficiency.

TABLE 4. Yields for the two analysis procedures.

	Neural Net	B Reconstruction
On	3013 ± 59	281 ± 17
Off (scaled)	2618 ± 73	155 ± 18
$\Upsilon(4s)$ background		
$b \to c$	50.7 ± 5.1	12 ± 2
$b \to u$	11.9 ± 4.0	2 ± 1
π^0 correction	50.2 ± 27.7	-0.7 ± 2.3
η correction	16.5 ± 33.7	2.0 ± 8.5
Non-$B\bar{B}$	2.3	
$\Upsilon(4s)$ total	132 ± 44	15 ± 9
On$-$Off$-\Upsilon(4S)$	263 ± 94	110 ± 25
	± 49	± 10

Our measured value is consistent with the Standard Model prediction[17,18] of $(2.75 \pm 0.80) \times 10^{-4}$, where the uncertainty is due to the effects discussed at the beginning of this section.

For the purposes of constraining extensions of the Standard Model, we have determined the 95% confidence level upper and lower limits to be:

$$1 \times 10^{-4} < Br(b \to s\gamma) < 4 \times 10^{-4}.$$

As one example, Fig. 26 shows the constraints on the charged Higgs mass as derived in the Two-Higgs-Doublet-Model II. The model has two parameters: the

charged Higgs mass, M_H, and the ratio of vacuum expectation values $\tan\beta = v_2/v_1$. A mass less than 260 GeV is excluded by our upper limit for all values of $\tan\beta$.
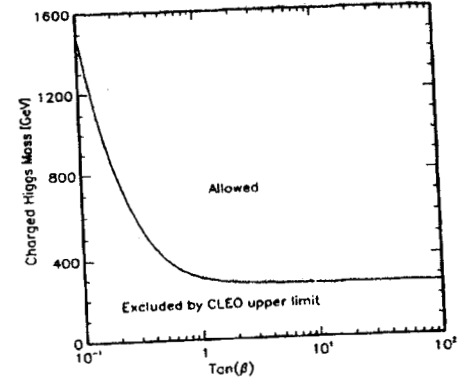

Figure 26. Upper limits on Higgs mass as a function of $\tan\beta$ in the Two-Higgs-Doublet-Model II. We have used $M_t = 175$ GeV. In addition, we have chosen the renormalization scale $\mu = 2m_b$ to make the Standard Model prediction as small as possible.

5 Summary

The important results presented in this paper can be summarized as follows:

1. Semileptonic Decays
   - $b_- = Br(\bar{B} \to Xl^-\nu) = (10.1 \pm 1.8 \pm 1.4)\%$. This is the first measurement of this branching fraction.
   - b_-/b_0 and f_{+-}/f_{00} are consistent with 1.
   - The measurement of $\bar{b} = Br(B \to Xe\nu)$ using lepton tags gives a model–independent result of $(10.36 \pm 0.17 \pm 0.40)\%$.
   - $Br(\Upsilon(4s) \to \text{non-}B\bar{B}) < 0.04$ (95% confidence level).

- $Br(B \rightarrow Xl\nu) < 11\%$ in contrast with theoretical predictions of no less than 12.5%.
- New measurements of $Br(B \rightarrow D^*l\nu)$ combined with HQET provide a reduced model-dependent value for $|V_{cb}| = 0.0377 \pm 0.0019 \pm 0.0024$.

2. Two-Body Hadronic Decays

- The factorization hypothesis seems to be valid for B decays, at least up to the a_1 mass.
- The BSW model gives a consistent picture for external and internal spectator decays.

3. Rare Decays

- Updated results for $B^0 \rightarrow \pi\pi / K\pi$ are consistent with our previous results.
- No signal has been observed in any other two-body hadronic modes. New upper limits, many in the 10^{-5} range, are presented for different modes. Several are close to the theoretical predictions.
- The branching fraction for $b \rightarrow s\gamma$ has been measured and is consistent with the Standard Model prediction. This measurement can constrain many extensions of the Standard Model. In the THDMII, the charged Higgs mass is constrained to be greater than 260 GeV.

Acknowledgments

References

[1] Particle Data Group, K. Hikasa et al., Phys. Rev. D **45**, No. 11, Pt. II (1992).

[2] CLEO Collaboration, S. Henderson et al., Phys. Rev. D **45**, 2212 (1992).

[3] CLEO Collaboration, J. Bartelt et al., "Inclusive Measurements of B Meson Semileptonic Branching Fractions," CLEO CONF 93-19.

[4] N. Isgur, D. Scora, B. Grinstein, and M.B. Wise, Phys. Rev. D **39**, 799 (1989).

[5] G. Altarelli, N. Cabibbo, G. Corbo, L. Maiani, and G. Martinelli, Nucl. Phys. **B208**, 365 (1982).

[6] This method was innovated by ARGUS. H. Albrecht et al., Phys. Lett. B **318**, 397 (1993).

[7] G. Altarelli and S. Petrarca, Phys. Lett. B **261** (1991); I. Bigi et al., UMN-TH 1225/93.

[8] N. Isgur and M. Wise, Phys. Lett. B **232**, 113 (1989).

[9] CLEO Collaboration, F. Butler et al., Phys. Rev. Lett. **69**, 2041 (1992).

[10] W. Venus, in: Lepton and Photon Interactions, XVI International Symposium, eds. Persis Drell and David Rubin, AIP Press, New York (1994).

[11] M. Neubert, SLAC Report No. SLAC-PUB-6263 (to appear in Physics Reports).

[12] M. Neubert, private communication. Ref. 11 gives F(1) = 0.986 ± 0.04, but the final version to appear in Physics Reports will have F(1) = 0.93 ± 0.04.

[13] M. Bauer, B. Stech, and M. Wirbel, Z. Phys. C **29**, 637 (1985); Z. Phys. C **34**, 103 (1987) and Z. Phys. C **42**, 671 (1989).

[14] CLEO Collaboration, M. Battle et al., Phys. Rev. Lett. **71**, 3922 (1993).

[15] A. Deandrea, N. Di Bartolomeo, R. Gatto, F. Feruglio, and G. Nardulli, Phys. Lett. B **320**, 170 (1994); N. G. Deshpande and Xiao-Gang He, OITS-538 (1994); A. Deandrea, N. Di Bartolomeo, R. Gatto, and G. Nardulli, Phys. Lett. B **318**, 549 (1993); A. J. Davies, T. Hayashi, M. Matsuda, and M. Tanimoto, AUE-02-93; L. L. Chau, H-Y Cheng, W. K. Sze, H. Yao, and B. Tseng, Phys. Rev. D **43**, 2176 (1991); N. G. Deshpande and J. Trampetic. Phys. Rev. D **41**, 895 (1990); M. Bauer, B. Stech, and M. Wirbel, Z. Phys. C **43**, 103 (1987).

[16] CLEO Collaboration, R. Ammar et al., Phys. Rev. Lett. **71**, 674 (1993).

[17] S. Bertolini et al., Phys. Rev. Lett. **59**, 180 (1987); N. Deshpande et al., Phys. Rev. Lett. **59**, 183 (1987); B. Grinstein et al., Phys. Lett. B **202**, 138 (1988); R. Grigjanis et al., Phys. Lett. B **224**, 209 (1989); G. Cella et al., Phys. Lett. B **248**. 181 (1990); A. J. Buras et al., Max Planck Institute preprint MPI-Ph/93-77.

[18] M. Ciuchini et al., CERN-TH 7283/94 (June 1994).

[19] J. L. Hewett, SLAC-PUB-6521 (May 1994).

[20] CLEO Collaboration, B. Barish et al., "First Measurement of the Inclusive Rate for the Radioactive Penguin Decays $b \rightarrow s\gamma$," ICHEP 94 Ref. GLS 0392, CLEO CONF 94-1.